



HAL
open science

New alkali lanthanide-free polyoxometalates with remarkable water-responsive turn-off–turn-on luminescence properties

Aurély Bagghi, Rania Ghena, Nicolas Gautier, Nicolas Stephant, Philippe Deniard, Rémi Dessapt

► To cite this version:

Aurély Bagghi, Rania Ghena, Nicolas Gautier, Nicolas Stephant, Philippe Deniard, et al.. New alkali lanthanide-free polyoxometalates with remarkable water-responsive turn-off–turn-on luminescence properties. *Journal of Materials Chemistry C*, 2022, 10 (42), pp.16040-16052. 10.1039/d2tc03038a . hal-03839819

HAL Id: hal-03839819

<https://hal.science/hal-03839819v1>

Submitted on 4 Nov 2022

HAL is a multi-disciplinary open access archive for the deposit and dissemination of scientific research documents, whether they are published or not. The documents may come from teaching and research institutions in France or abroad, or from public or private research centers.

L'archive ouverte pluridisciplinaire **HAL**, est destinée au dépôt et à la diffusion de documents scientifiques de niveau recherche, publiés ou non, émanant des établissements d'enseignement et de recherche français ou étrangers, des laboratoires publics ou privés.

New Alkali Lanthanide-free Polyoxometalates with Remarkable Water-Responsive Turn-Off-Turn-On Luminescence Properties

Aurély Bagghi, Rania Ghena, Nicolas Gautier, Nicolas Stephant, Philippe Deniard,* Rémi Dessapt*

Received 00th January 20xx,
Accepted 00th January 20xx

DOI: 10.1039/x0xx00000x

Three new water-responsive luminescent lanthanide-free polyoxometalate (Ln-free POM) materials $\text{Na}_7[\text{SbW}_6\text{O}_{24}]$, $\text{K}_5\text{Na}_2[\text{SbW}_6\text{O}_{24}]$ and $\text{K}_7[\text{SbW}_6\text{O}_{24}]$ were prepared by thermally dehydrating the known compounds $\text{Na}_7[\text{SbW}_6\text{O}_{24}] \cdot 16\text{H}_2\text{O}$, $\text{K}_5\text{Na}_2[\text{SbW}_6\text{O}_{24}] \cdot 12\text{H}_2\text{O}$, and a new one $\text{K}_7[\text{SbW}_6\text{O}_{24}] \cdot 6\text{H}_2\text{O}$. The isostructural anhydrous phases have been fully characterized by a combination of techniques (High Temperature Powder X-Ray Diffraction (HT-PXRD), thermal analyses, scanning electron microscopy (SEM), FT-IR, FT-Raman, UV-vis and photoluminescence (PL) spectroscopies), and their structures have been solved from ab initio powder X-ray diffraction determination. The PL properties of these materials are reversibly tunable by controlling their hydration degree. The three hydrated compounds are barely or nonluminescent at room temperature because water molecules promote non-radiative deactivation processes from the emitting levels of the $[\text{SbW}_6\text{O}_{24}]^{7-}$ unit. However, the anhydrous phases show remarkable PL enhancement. The PL quantum yields vary with the nature of the alkali ions, and $\text{Na}_7[\text{SbW}_6\text{O}_{24}]$ exhibits the best performances of this series. These materials also exhibit highly efficient turn-off vapoluminescence properties upon exposure to a humid atmosphere. They are fully converted into their parent hydrates, resulting in strong and complete PL quenching effects. The rehydration kinetics are much faster for the K^+ -containing materials, which could be interpreted taking into account of structural filiations between anhydrous and hydrated compounds. Finally, the complete regeneration of the PL-active anhydrous phases can be achieved by simple thermal dehydration.

INTRODUCTION

Polyoxometalates^{1,2} (POMs) are metal-oxide anionic clusters of early transition metals (usually Mo, W, V) whose redox and optical properties can be finely tuned according to their chemical composition, charge, shape and size. They are currently undergoing a remarkable development these last decades, due to their high relevance in many domains connected to materials science including single molecule magnets (SMMs),^{3,4} photochromism,^{5,6} catalysis,⁷ photocatalysis^{8–10} and photoluminescence (PL) sensing.^{11,12} In this very active field, polyoxometalates incorporating visible-emitting lanthanide Ln^{3+} ions (Ln-POMs)^{13–17} have been intensively investigated to design stimuli-responsive luminescent materials and sensors for luminescence thermometry,^{18,14} anticounterfeiting and luminescence security printing,¹⁹ and luminescence bio-sensing.^{20,21} In most of cases, the POM ligands act as sensitizers to enhance the emission of the Ln^{3+} ions via an antenna effect,^{22,23} in which the photoexcitation into the high energy O→M ligand-to-metal charge transfer (LMCT) bands is followed by intramolecular POM-to- Ln^{3+} energy transfers and emission processes due to f-f transitions within the Ln^{3+} ions. The Weakley-type $[\text{Eu}(\text{W}_5\text{O}_{18})_2]^{9-}$ polyoxotungstate²⁴ is a very efficient emitter at room temperature which has been exploited to elaborate a wide range of chemical probes for the detection of analytes in water i.e., heavy metal cations,²⁵ H_2O_2 ,²⁶ amines,²⁷ human papillomavirus,²⁹ and enzymes.²⁹ In contrast, its integration into PL sensors able to detect trace levels of water in liquids or gas has been much more scarcely reported.³⁰ However, the design of new Ln-POMs exhibiting high PL properties at room temperature is still highly challenging, and very few candidates fulfill all required structural and electronic criteria.³¹ In particular, only the

Ln^{3+} ions with an emitting level lying in the O→M LMCT bands are able to undergo efficient POM-to- Ln^{3+} energy transfers,^{31,32} which dramatically restrains the choice of suitable Ln^{3+} /POM combinations. Moreover, considering rising costs associated with the difficulties of extracting or recycling rare earths, water-responsive Ln-free POM luminescent materials could be a promising lower-cost alternative.

Very recently, two Ln-free Keggin-type POMs incorporating Bi^{3+} and Pb^{2+} ions as emitting centers were reported as crystallographically uncharacterized tetrabutylammonium salts.³³ They demonstrated reversible solid-state vapoluminescent properties in the presence of water vapor, involving an emission color change between wet and dry samples. Many other PL Ln-free POMs have already been elaborated since the 1990s,^{34–36} essentially as hydrated alkali salts. Their solid-state emission originates directly from the O→M LMCT triplet levels, or after intramolecular energy transfers, from discrete energy levels lower in energy than the LMCT states, for POMs containing additional transition metal ions (Cr^{3+} , Mn^{4+} ...),³⁴ However, these compounds have been very scarcely exploited in materials science,³⁷ essentially because most of them are luminescent only at low temperatures (below 100 K). Indeed, the crystallized water molecules form an extended hydrogen-bonding network connecting the oxygen POM surface, and O-H vibrators are responsible for strong PL quenching at room temperature by promoting non-radiative deactivation processes from the emitting levels.^{34,36} The Anderson-type $[\text{SbW}_6\text{O}_{24}]^{7-}$ unit is one of the most performant PL Ln-free POMs,³⁵ and its potassium salt $\text{K}_{5.5}\text{H}_{1.5}[\text{SbW}_6\text{O}_{24}] \cdot 6\text{H}_2\text{O}$ ³⁸ exhibits a green luminescence which is even distinguishable with naked eyes below room temperature. Two other hydrates have been also reported,^{39,40} but their PL properties remain still uninvestigated.

Herein, we postulate that the solid-state emission of alkali $[\text{SbW}_6\text{O}_{24}]^{7-}$ -containing materials could be reversibly tuned by controlling their hydration degree. As a proof of concept, we report a complete study of the precise impact of thermal dehydration/rehydration processes on the structure, the particles size and morphology, and the photophysical properties of $\text{Na}_7[\text{SbW}_6\text{O}_{24}] \cdot 16\text{H}_2\text{O}$,³⁹ $\text{K}_5\text{Na}_2[\text{SbW}_6\text{O}_{24}] \cdot 12\text{H}_2\text{O}$,⁴⁰ and the new compound $\text{K}_7[\text{SbW}_6\text{O}_{24}] \cdot 6\text{H}_2\text{O}$. First, the thermal behaviors of the three hydrates have been fully investigated by a combination of

Nantes Université, CNRS, Institut des Matériaux de Nantes Jean Rouxel, IMN, F-44000 Nantes, France. E-mail: remi.dessapt@cnrs-imn.fr, philippe.deniard@cnrs-imn.fr

Electronic Supplementary Information (ESI) available: Additional PXRD patterns, FT-IR and FT-Raman spectra, TGA/DSC measurements, S/TEM-EDS spectrum, SEM images, crystallographic data and refinements parameters, room-temperature solid-state UV-vis absorption, PL and PLE spectra, CIE chromaticity diagrams, and luminescence decay curves of the hydrated and anhydrous materials. CIF files of the three new anhydrous materials. See DOI: 10.1039/x0xx00000x

thermogravimetric measurements, High Temperature Powder X-Ray Diffraction (HT-PXRD) analysis, scanning electron microscopy (SEM), FT-IR and FT-Raman spectroscopies. Their complete thermal dehydration has led to three new isostructural anhydrous phases namely, $\text{Na}_7[\text{SbW}_6\text{O}_{24}]$, $\text{K}_5\text{Na}_2[\text{SbW}_6\text{O}_{24}]$, and $\text{K}_7[\text{SbW}_6\text{O}_{24}]$, and their crystal structures have been solved from *ab initio* powder X-ray diffraction determination. Then, the room-temperature solid-state absorption and PL properties of both hydrated and anhydrous series have been thoroughly investigated, and structure-property relationships have been evidenced. As envisaged, the thermal dehydration processes cause a tremendous emission enhancement, and PL quantum efficiencies depend on the nature of the alkali ions. Moreover, it is demonstrated here that the luminescence properties of the anhydrous phases at room temperature are highly tunable with the presence of humidity in the atmosphere. Exposure to moisture-laden air induces strong PL quenching effects which are due to the complete regeneration of the hydrated parent salts, the rehydration rates varying with the structures of the hydrates. The anhydrous phases are then easily regenerated by soft thermal treatments, making them highly efficient sustainable and reusable water-responsive luminescent materials.

RESULTS AND DISCUSSION

1. Hydrated alkali Ln-free POM materials: $\text{Na}_7[\text{SbW}_6\text{O}_{24}]\cdot 16\text{H}_2\text{O}$, $\text{K}_5\text{Na}_2[\text{SbW}_6\text{O}_{24}]\cdot 12\text{H}_2\text{O}$ and $\text{K}_7[\text{SbW}_6\text{O}_{24}]\cdot 6\text{H}_2\text{O}$

1.1. Synthesis

The microcrystalline powder of $\text{K}_5\text{Na}_2[\text{SbW}_6\text{O}_{24}]\cdot 12\text{H}_2\text{O}$ has been elaborated in water from a one-step synthesis procedure inspired from that previously reported,⁴⁰ using K_2WO_4 and $\text{KSb}(\text{OH})_6$ as W and Sb sources, respectively. Single crystals of $\text{Na}_7[\text{SbW}_6\text{O}_{24}]\cdot 16\text{H}_2\text{O}$ ³⁹ have been obtained from a new synthetic route using $\text{Na}_2\text{WO}_4\cdot 2\text{H}_2\text{O}$, and SbCl_5 instead of $\text{KSb}(\text{OH})_6$ to avoid the formation of $\text{K}_5\text{Na}_2[\text{SbW}_6\text{O}_{24}]\cdot 12\text{H}_2\text{O}$ as impurity. The powder X-ray diffraction (PXRD) patterns of both hydrated materials match well their structural models (Fig. S1, ESI[†]). The new $\text{K}_7[\text{SbW}_6\text{O}_{24}]\cdot 6\text{H}_2\text{O}$ compound has been elaborated from a synthesis protocol adapted from that of $\text{K}_5\text{Na}_2[\text{SbW}_6\text{O}_{24}]\cdot 12\text{H}_2\text{O}$, without adding NaCl in the aqueous medium. The obtained crystals were efflorescent, and attempts to solve their structure by single-crystal X-ray diffraction analysis were unsuccessful even at low temperature. Let us notice that their PXRD pattern (Fig. S2, ESI[†]) differs from that of $\text{K}_{5.5}\text{H}_{1.5}[\text{SbW}_6\text{O}_{24}]\cdot 6\text{H}_2\text{O}$.³⁸ The presence of the $[\text{SbW}_6\text{O}_{24}]^{7-}$ unit in $\text{K}_7[\text{SbW}_6\text{O}_{24}]\cdot 6\text{H}_2\text{O}$ has been evidenced by comparing its FT-IR spectrum with those of $\text{Na}_7[\text{SbW}_6\text{O}_{24}]\cdot 16\text{H}_2\text{O}$ and $\text{K}_5\text{Na}_2[\text{SbW}_6\text{O}_{24}]\cdot 12\text{H}_2\text{O}$ (Fig. S3, ESI[†]). In addition, the K/Sb, K/W and W/Sb elemental ratios in $\text{K}_7[\text{SbW}_6\text{O}_{24}]\cdot 6\text{H}_2\text{O}$ were determined by Scanning Transmission Electron Microscopy (S/TEM) and Energy Dispersive X-ray Spectroscopy (EDS) analyses (Fig. S4, ESI[†]) and are equal to 6.9, 1.2 and 6.0, respectively, in very good agreement with the expected ones. Finally, the hydration degree i.e., the quantity of crystallized water molecules has been determined from thermogravimetric analysis (see section 1.3).

1.2. Structural descriptions of $\text{Na}_7[\text{SbW}_6\text{O}_{24}]\cdot 16\text{H}_2\text{O}$ and $\text{K}_5\text{Na}_2[\text{SbW}_6\text{O}_{24}]\cdot 12\text{H}_2\text{O}$

The crystal structures of $\text{Na}_7[\text{SbW}_6\text{O}_{24}]\cdot 16\text{H}_2\text{O}$ and $\text{K}_5\text{Na}_2[\text{SbW}_6\text{O}_{24}]\cdot 12\text{H}_2\text{O}$ are depicted in Fig. 1, and briefly described as followed. Both compounds contain the Anderson-Evans-type $[\text{SbW}_6\text{O}_{24}]^{7-}$ polyanion which is built upon a Sb^{5+} ion in a central cavity of the crown formed by six edge-shared $\{\text{WO}_6\}$ octahedra (Fig. 1a). In each compound, the $[\text{SbW}_6\text{O}_{24}]^{7-}$ entities are assembled with alkali

ions and water molecules in numerous hydrogen bonding interactions. $\text{Na}_7[\text{SbW}_6\text{O}_{24}]\cdot 16\text{H}_2\text{O}$ crystallizes in the $P\bar{1}$ space group. The $[\text{SbW}_6\text{O}_{24}]^{7-}$ anions connect $\{\text{Na}_6\text{O}_8\cdot 14\text{H}_2\text{O}\}$ formal clusters into supramolecular layers in the (*ab*) plane (Fig. 1b). The sodium clusters are formed by six edge-shared $\{\text{NaO}_6\}$ octahedra involving oxo ligands of adjacent POMs and water molecules. These latter link the POM surface via eighteen H-bonds (with O...O distances ranging from 2.66 to 2.95 Å) with six oxo ligands of the central $\{\text{SbO}_6\}$ octahedron, and eight terminal and bridging μ_2 -oxo ligands of the $\{\text{W}_6\text{O}_{18}\}$ ring (Fig. 1b and Fig. S5, ESI[†]). The supramolecular layers are stacked along the *c*-axis and are connected by $\{\text{NaO}_4(\text{H}_2\text{O})_2\}$ octahedra involving four terminal oxo ligands of two adjacent POMs (Fig. 1c). Each POM anion also links two sodium clusters of neighboring layers via two H-bonds (O...O distance of 2.80 Å) (Fig. S5, ESI[†]). Finally, additional water molecules not directly interacting with Na^+ ions are localized between the layers, and link the POM surface via two other H-bonds (O...O distance of 2.72 Å).

$\text{K}_5\text{Na}_2[\text{SbW}_6\text{O}_{24}]\cdot 12\text{H}_2\text{O}$ crystallizes in the $R\bar{3}m$ space group. Its crystal lattice is described herein in the hexagonal metric to facilitate the comparison with that of its anhydrous homologue (see section 2.1.). The $[\text{SbW}_6\text{O}_{24}]^{7-}$ units form a hexagonal arrangement and are assembled with Na^+ cations and water molecules into supramolecular layers in the (*ab*) plane (Fig. 1d). These latter are stacked along the *c*-axis, and separated by the larger K^+ ions. Each POM anion is surrounded by six $[\text{Na}(\text{H}_2\text{O})_6]^+$ octahedra forming a honeycomb-like arrangement. The $[\text{Na}(\text{H}_2\text{O})_6]^+$ entities connect the POM surface via eighteen H-bonds (O...O distances of 2.68 and 2.95 Å) which involve all terminal and bridging μ_2 -oxo ligands of the $\{\text{W}_6\text{O}_{18}\}$ ring. Along the *c*-axis, two $[\text{Na}(\text{H}_2\text{O})_6]^+$ cations of neighboring layers also connect the POM surface via six other H-bonds (O...O distance of 2.90 Å), involving only the μ_2 -oxo ligands (Fig. 1e).

1.3. Thermal dehydration study

The thermal behaviors of the three hydrated materials have been investigated by a combination of thermal and HT-PXRD analyses. The thermogravimetric analysis (TGA) and differential scanning calorimetry (DSC) curves of $\text{Na}_7[\text{SbW}_6\text{O}_{24}]\cdot 16\text{H}_2\text{O}$ (Fig. 2a) show a weight loss of 13.61 % upon heating between room temperature and 120 °C, which is well consistent with expected removal of the sixteen crystallized water molecules (theoretical weight loss of 14.01 %). This proceeds in three distinct steps characterized by sharp endothermic peaks in the DSC curve. A first weight loss (4.70 %) is observed in the temperature range of 46–74 °C, and is attributed to the removal of six water molecules (theoretical weight loss of 5.24 %). A second weight loss (5.31 %) occurs between 74 and 110 °C which corresponds to the removal of six other ones. The third weight loss (3.60 %) in the temperature range of 110–120 °C is attributed to the removal of the last four water molecules (theoretical weight loss of 3.50 %), leading to a new anhydrous $\text{Na}_7[\text{SbW}_6\text{O}_{24}]$ material. These results clearly evidenced that, when progressively increased the temperature, the complete thermal dehydration process of $\text{Na}_7[\text{SbW}_6\text{O}_{24}]\cdot 16\text{H}_2\text{O}$ involves the gradual formation of two new compounds with intermediary hydration degrees, namely $\text{Na}_7[\text{SbW}_6\text{O}_{24}]\cdot 10\text{H}_2\text{O}$ and $\text{Na}_7[\text{SbW}_6\text{O}_{24}]\cdot 4\text{H}_2\text{O}$. Their structural and photophysical properties are beyond the scope of our present study and will be subject to further investigations in our future work. No weight loss occurs from 120 °C and 700 °C which corresponds to the melting point of $\text{Na}_7[\text{SbW}_6\text{O}_{24}]$, well characterized by a sharp endothermic peak on the DSC curve. Noticeably, a broad exothermic peak is observed in the 400–650 °C range which has been attributed to the progressive crystallization process of the anhydrous phase.

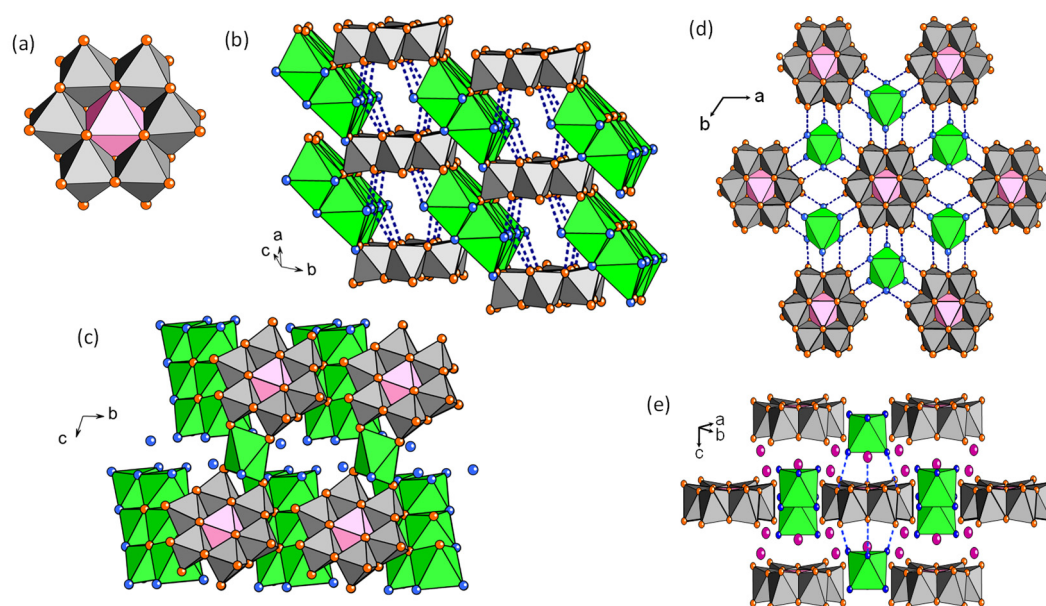


Fig 1. (a) Polyhedral representation of the $[\text{SbW}_6\text{O}_{24}]^{7-}$ POM. (b) and (c) Crystal packing in $\text{Na}_7[\text{SbW}_6\text{O}_{24}] \cdot 16\text{H}_2\text{O}$. (d) and (e) Crystal packing in $\text{K}_5\text{Na}_2[\text{SbW}_6\text{O}_{24}] \cdot 12\text{H}_2\text{O}$ (grey octahedra: WO_6 , pink octahedra: SbO_6 , green octahedra: NaO_6 , orange sphere: oxygen atoms of the POM unit, blue sphere: oxygen atoms of water molecules, purple sphere: potassium. H-bonding interactions are displayed as blue dotted lines. H atoms are not displayed).

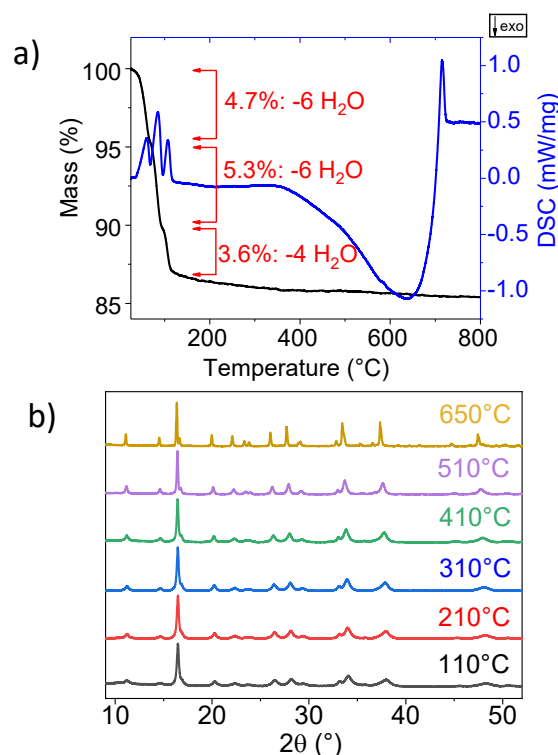


Fig 2 (a) TGA (black) and DSC (blue) curves of $\text{Na}_7[\text{SbW}_6\text{O}_{24}] \cdot 16\text{H}_2\text{O}$. (b) PXRD patterns of $\text{Na}_7[\text{SbW}_6\text{O}_{24}]$ upon heating between 110 °C and 650 °C

This has been unambiguously evidenced by performing PXRD analysis at different temperatures, between 110 °C and 650 °C (Fig.

2b). The PXRD patterns of $\text{Na}_7[\text{SbW}_6\text{O}_{24}]$ exhibit a progressive sharpening of the diffraction peaks with increasing the temperature, and no additional crystallized phase has been detected. This confirms that $\text{Na}_7[\text{SbW}_6\text{O}_{24}]$ is thermally robust in the considered temperature range. Similar thermal analyses have been performed on $\text{K}_5\text{Na}_2[\text{SbW}_6\text{O}_{24}] \cdot 12\text{H}_2\text{O}$ (Fig. S6, ESI⁺) and $\text{K}_7[\text{SbW}_6\text{O}_{24}] \cdot 6\text{H}_2\text{O}$ (Fig. S7, ESI⁺). The TGA/DSC curves indicates that full removal of the crystallized water molecules occurs in the temperature range of 25-110 °C for $\text{K}_5\text{Na}_2[\text{SbW}_6\text{O}_{24}] \cdot 12\text{H}_2\text{O}$, and of 25-150 °C for $\text{K}_7[\text{SbW}_6\text{O}_{24}] \cdot 6\text{H}_2\text{O}$. In each case, the weight loss proceeds in two steps, characterized by two distinguishable endothermic peaks in the DSC curves, which reveals the formation of an intermediary hydrate (not considered herein) before reaching the new anhydrous phase. Then, the melting of $\text{K}_5\text{Na}_2[\text{SbW}_6\text{O}_{24}]$ and $\text{K}_7[\text{SbW}_6\text{O}_{24}]$ occurs at 580 °C and 598 °C, respectively, indicating that they are less thermally robust than $\text{Na}_7[\text{SbW}_6\text{O}_{24}]$. Noticeably, the PXRD patterns of $\text{Na}_7[\text{SbW}_6\text{O}_{24}]$, $\text{K}_5\text{Na}_2[\text{SbW}_6\text{O}_{24}]$ and $\text{K}_7[\text{SbW}_6\text{O}_{24}]$ recorded at high temperatures show strong similarities (Fig. S8, ESI⁺), suggesting that the three anhydrous phases are isostructural.

2- Anhydrous alkali Ln-free POM materials: $\text{Na}_7[\text{SbW}_6\text{O}_{24}]$, $\text{K}_5\text{Na}_2[\text{SbW}_6\text{O}_{24}]$ and $\text{K}_7[\text{SbW}_6\text{O}_{24}]$

2.1. Crystal structures

The structures of $\text{Na}_7[\text{SbW}_6\text{O}_{24}]$, $\text{K}_5\text{Na}_2[\text{SbW}_6\text{O}_{24}]$ and $\text{K}_7[\text{SbW}_6\text{O}_{24}]$ have been solved from *ab initio* powder X-ray diffraction determination and refined by the Rietveld method.⁴² The determination of the structural model of the three compounds was first started with the pattern of $\text{Na}_7[\text{SbW}_6\text{O}_{24}]$ at 650 °C. As the structure factor of these compounds is largely dominated by the $[\text{SbW}_6\text{O}_{24}]^{7-}$ cluster, it was decided to use this information as a rigid body to build the structural model. The cluster model was taken from

the crystal structure of $\text{Na}_7[\text{SbW}_6\text{O}_{24}] \cdot 16\text{H}_2\text{O}$.³⁹ At this point, it was assumed that this cluster is robust enough to not vary too much from one structure to another. In addition, it is supposed to be not very sensitive to temperature variation to fit with the above mentioned patterns recorded at high temperature. A hexagonal unit cell for $\text{Na}_7[\text{SbW}_6\text{O}_{24}]$ was found using Expo2014 software⁴³ thanks to an embedded version of Dicvol06.⁴⁴ The difficulty to find unambiguously a space group from systematic extinctions let us consider to use, in the $P1$ space group, the hexagonal cell parameters found previously (the symmetry being later determined in the direct space). At this point, a measured density of the compound (5.67 g/cm^3) in regard of the cell volume led to 3 formula units per hexagonal unit cell. The above mentioned cluster was introduced in Fox software⁴⁵ thanks to a Fenske-Hall matrix transformation, in the $P1$ space group. The as-obtained partial structural model introduced in JANA2020 as a rigid body was completed by difference Fourier maps prior to use individual atom positions. At the end of the procedure, the symmetry was found to correspond to the $R\bar{3}$ space group. Although the structure determination was first obtained from high temperature patterns, the following structure description is given for $\text{Na}_7[\text{SbW}_6\text{O}_{24}]$ and $\text{K}_7[\text{SbW}_6\text{O}_{24}]$ after cooling down to 30°C during HT-PXRD experiment. All the procedure was done under dry nitrogen atmosphere to avoid any rehydration. However, despite these precautions and may be because of its highly fast reactivity towards humidity (see below), this could not be achieved for $\text{K}_5\text{Na}_2[\text{SbW}_6\text{O}_{24}]$. Thus, its structure reported in ESI† is that of a data collection at 500°C . Due to the structure factor largely dominated by the tungsten and

antimony atoms, sodium Atomic Displacement Parameters (ADP) were constrained as well as all of those of the oxygen atoms. Fig. 3 shows the observed, calculated and difference patterns for $\text{Na}_7[\text{SbW}_6\text{O}_{24}]$ and Table 1 shows the complete description of its structural model.

The structure of $\text{Na}_7[\text{SbW}_6\text{O}_{24}]$ is displayed in Fig. 4, and it has been arbitrary chosen to describe the crystal packing in the series of isostructural anhydrous phases. The $[\text{SbW}_6\text{O}_{24}]^{7-}$ units are arranged into hexagonal supramolecular layered networks in the (ab) plane (Fig. 4a), and are in closed proximity. The shortest intermolecular O...O distance is of $3.094(18) \text{ \AA}$, indicating significant electrostatic anion-anion interactions. The POM layers are stacked along the c -axis and separated by alkali ions (Fig. 4b) which occupy two distinct Wyckoff positions (Table 1). In the first one (3b), the Na^+ ions are surrounded by six O-atoms in a regular octahedral environment (Fig. 4c). In the second one (18f), they are surrounded by seven O-atoms and occupy a distorted monocapped trigonal prismatic site (Fig. 4d). The same structural model has been used for $\text{K}_5\text{Na}_2[\text{SbW}_6\text{O}_{24}]$ and $\text{K}_7[\text{SbW}_6\text{O}_{24}]$ and the results of the Rietveld refinements are reported in Table S1, ESI† and Table S2, ESI†, and displayed in Fig. S9, ESI† and Fig. S10, ESI†, respectively. Let us notice that, in the crystal structure of $\text{K}_5\text{Na}_2[\text{SbW}_6\text{O}_{24}]$, the 3b Wyckoff position is solely occupied by K^+ ions while the 18f Wyckoff position is randomly occupied by both K^+ and Na^+ ions with a site occupation fraction of about 0.72 and 0.28, respectively.

Table 1. Atom positions, site occupation fraction and atomic displacement parameters of $\text{Na}_7[\text{SbW}_6\text{O}_{24}]$ at 30°C .

S.G. $R\bar{3}$, $a(\text{\AA}) = 10.53600(18)$, $c(\text{\AA}) = 16.1942(5)$, $R_{\text{Bragg}} = 3.60$, $\text{GOF} = 1.31$, $R_{\text{wp}} = 10.74$						
atom	x	y	z	SOF	Wyckoff	$U_{\text{iso}} (\text{\AA}^2)$
Na1	0	0	0.5	1	3b	0.021(3)
Na2	0.1110(12)	0.2729(10)	0.1862(6)	1	18f	0.021(3)
O1	0.520(2)	0.1774(17)	0.4010(9)	1	18f	0.016(3)
O2	-0.048(2)	-0.363(2)	0.3964(11)	1	18f	0.016(3)
O3	0.1889(15)	0.1389(17)	0.2454(12)	1	18f	0.016(3)
O4	0.200(2)	-0.003(2)	0.4125(10)	1	18f	0.016(3)
Sb1	0	0	0	1	3a	0.0025(18)
W1	-0.17427(16)	-0.31023(14)	0.33367(11)	1	18f	0.0139(13)
* $U_{\text{aniso}}(\text{W1})$: 0.0055(16); 0.018(2); 0.0152(9); 0.0041(10); 0.008(2); 0.0052(16)						

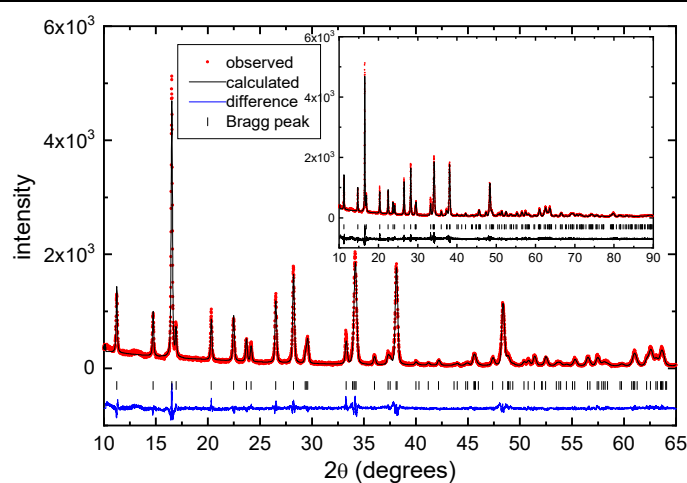


Fig. 3 Observed, refined and difference patterns of $\text{Na}_7[\text{SbW}_6\text{O}_{24}]$ after Rietveld refinement ($R_{\text{Bragg}} = 3.60$, $\text{GOF} = 1.31$, $R_{\text{wp}} = 10.74$).

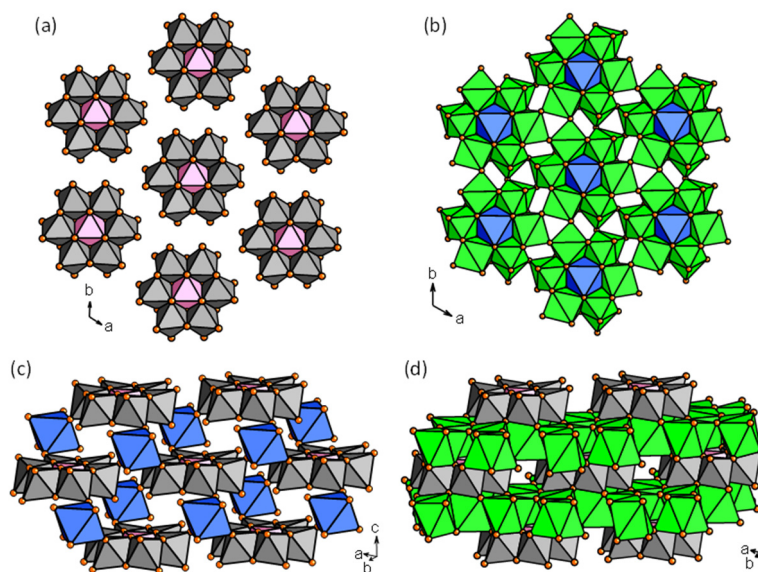


Fig. 4 Polyhedral representations of the crystal packing in $\text{Na}_7[\text{SbW}_6\text{O}_{24}]$. (a) Supramolecular layers of (a) the $[\text{SbW}_6\text{O}_{24}]^{7-}$ units and (b) the $\{\text{NaO}_6\}$ and $\{\text{NaO}_7\}$ polyhedra in the (ab) plane. (c) Stacking of the POM layers and the Na^+ ions in (c) the 3b and (d) the 18f Wyckoff positions (grey octahedra: WO_6 , pink octahedra: SbO_6 , blue octahedra: NaO_6 , green octahedra: NaO_7 , orange sphere: oxygen).

Very interestingly, the supramolecular hexagonal networks of POMs and alkali ions alternated along the c -axis shows significant similarities with those observed in $\text{K}_5\text{Na}_2[\text{SbW}_6\text{O}_{24}] \cdot 12\text{H}_2\text{O}$ (section 1.2.), suggesting that structural filiation could exist between the anhydrous material and its parent hydrate. In contrast, no apparent correlations between the structures of $\text{Na}_7[\text{SbW}_6\text{O}_{24}]$ and $\text{Na}_7[\text{SbW}_6\text{O}_{24}] \cdot 16\text{H}_2\text{O}$ have been evidenced.

2.2. FTIR-ATR and FT-Raman characterizations

Based on results of the thermal analysis, powder samples of $\text{Na}_7[\text{SbW}_6\text{O}_{24}]$, $\text{K}_5\text{Na}_2[\text{SbW}_6\text{O}_{24}]$ and $\text{K}_7[\text{SbW}_6\text{O}_{24}]$ have been elaborated by thermally dehydrating their hydrated homologues at 200°C for 10 minutes. Then, the anhydrous phases have been characterized by infrared and Raman spectroscopies. As an example, the FTIR-ATR and Raman spectra of $\text{Na}_7[\text{SbW}_6\text{O}_{24}]$ are displayed in Fig. 5, in comparison with those of $\text{Na}_7[\text{SbW}_6\text{O}_{24}] \cdot 16\text{H}_2\text{O}$. As expected, the vibration bands of water molecules around 3500 cm^{-1} (OH-stretching modes) and 1600 cm^{-1} (HOH-bending modes) in the FTIR-ATR spectrum of $\text{Na}_7[\text{SbW}_6\text{O}_{24}] \cdot 16\text{H}_2\text{O}$ are not observed in that of $\text{Na}_7[\text{SbW}_6\text{O}_{24}]$ (Fig. 5a). Both spectra show the vibrational signature of $[\text{SbW}_6\text{O}_{24}]^{7-}$ in the range $1000\text{--}400\text{ cm}^{-1}$. The bands corresponding to the pure stretching $\nu_{\text{as}}(\text{W}=\text{O})$ modes involving terminal oxo ligands are observed at 866 cm^{-1} and 932 cm^{-1} in $\text{Na}_7[\text{SbW}_6\text{O}_{24}] \cdot 16\text{H}_2\text{O}$ and are slightly shifted at higher frequencies (872 cm^{-1} and 953 cm^{-1}) in $\text{Na}_7[\text{SbW}_6\text{O}_{24}]$. This can be explained considering that the $\text{W}=\text{O}$ bonds at the surface of $[\text{SbW}_6\text{O}_{24}]^{7-}$ are involved in many H-bonding interactions with the water molecules in $\text{Na}_7[\text{SbW}_6\text{O}_{24}] \cdot 16\text{H}_2\text{O}$ (see section 1.2). Thus, the thermal treatment suppresses the H-bonding network resulting in an increase of the $\nu_{\text{as}}(\text{W}=\text{O})$ frequencies.^{46,47}

The FT-Raman spectroscopy has been also used as a powerful complementary tool to confirm that the integrity of the POM is maintained after thermal dehydration. The Raman spectrum of $\text{Na}_7[\text{SbW}_6\text{O}_{24}] \cdot 16\text{H}_2\text{O}$ (Fig. 5b) shows several peaks in the $50\text{--}800\text{ cm}^{-1}$ range, corresponding to the $\text{W}-\text{O}$ and $\text{Sb}-\text{O}$ bonds involving μ_2 -oxo

and μ_3 -oxo bridges of the $[\text{SbW}_6\text{O}_{24}]^{7-}$ unit.⁴⁸ Among them, the bands at 590 and 676 cm^{-1} can be assigned to both stretching $\text{W}-\text{O}$ and $\text{Sb}-\text{O}$ modes.

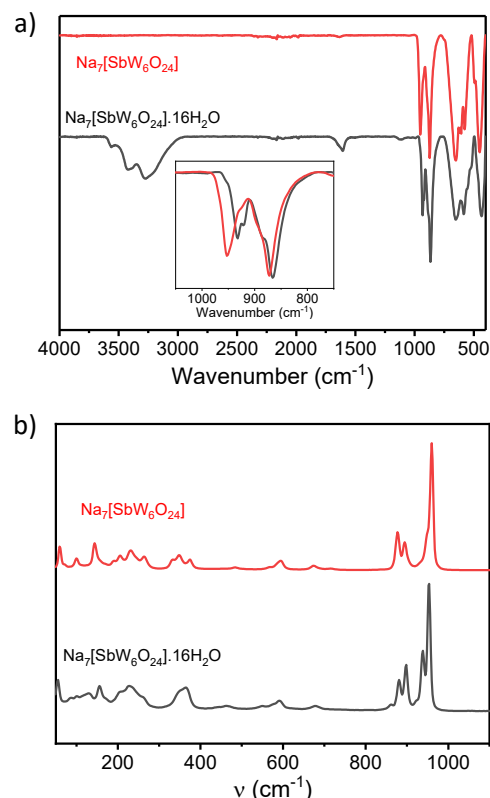


Fig. 5 (a) FTIR-ATR spectra of $\text{Na}_7[\text{SbW}_6\text{O}_{24}]$ (red line) and $\text{Na}_7[\text{SbW}_6\text{O}_{24}] \cdot 16\text{H}_2\text{O}$ (black line). (b) FT-Raman spectra of $\text{Na}_7[\text{SbW}_6\text{O}_{24}]$ (red line) and $\text{Na}_7[\text{SbW}_6\text{O}_{24}] \cdot 16\text{H}_2\text{O}$ (black line).

Four more intense bands are observed at 881 , 898 , 939 and 954 cm^{-1} which correspond to the stretching modes of the shorter $\text{W}=\text{O}$

bonds. The FT-Raman spectra of $\text{Na}_7[\text{SbW}_6\text{O}_{24}]$ is comparable with that of $\text{Na}_7[\text{SbW}_6\text{O}_{24}] \cdot 16\text{H}_2\text{O}$, and in particular, the four main lines in the range $800\text{--}1000\text{ cm}^{-1}$ are clearly distinguishable. Similar results have been obtained by comparing the FTIR-ATR (Fig. S11, ESI[†]) and FT-Raman (Fig. S12, ESI[†]) spectra of $\text{K}_5\text{Na}_2[\text{SbW}_6\text{O}_{24}]$ and $\text{K}_7[\text{SbW}_6\text{O}_{24}]$ with those of their hydrates.

2.3. Rehydration and deuteration processes

The rehydration capacity of the three anhydrous materials in moisture-laden air has been investigated. The freshly thermally dehydrated powder samples were kept for three days at room temperature, in a closed chamber with a high relative humidity (RH) level of 100%. Then, the samples were characterized by PXRD and thermal analyses. As shown in Fig. 6, the PXRD pattern of $\text{Na}_7[\text{SbW}_6\text{O}_{24}]$ after rehydration is strictly similar to that of $\text{Na}_7[\text{SbW}_6\text{O}_{24}] \cdot 16\text{H}_2\text{O}$, and no remaining peaks of the anhydrous phase are observed. The TGA curve of the rehydrated $\text{Na}_7[\text{SbW}_6\text{O}_{24}]$ also shows that the weight loss observed in the $25\text{--}200\text{ }^\circ\text{C}$ range is consistent with the removal of sixteen water molecules (Fig. S13, ESI[†]), confirming that the rehydration process is complete. Similar results have been obtained for $\text{K}_5\text{Na}_2[\text{SbW}_6\text{O}_{24}]$ and $\text{K}_7[\text{SbW}_6\text{O}_{24}]$ (Fig. S14, ESI[†]) which well evidence the full regeneration of $\text{K}_5\text{Na}_2[\text{SbW}_6\text{O}_{24}] \cdot 12\text{H}_2\text{O}$ and $\text{K}_7[\text{SbW}_6\text{O}_{24}] \cdot 6\text{H}_2\text{O}$. Noticeably, the rehydration processes are perfectly reversible, and the initial anhydrous phases can be then easily reset again by a simple thermal treatment at $200\text{ }^\circ\text{C}$ for 10 minutes. In addition, these materials

exhibit a good cyclability over successive dehydration/hydration processes (Fig. S15, ESI[†]).

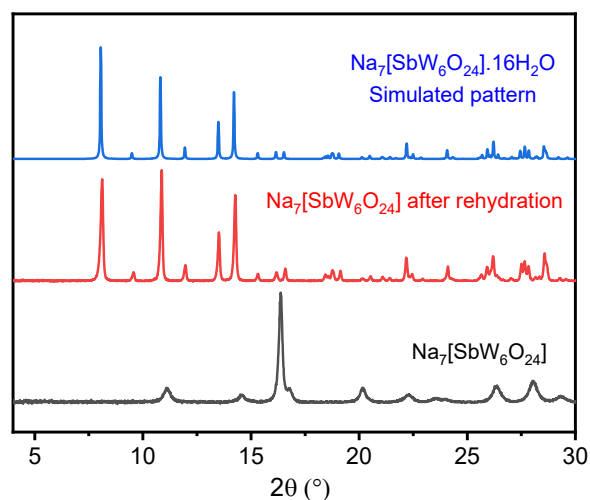


Fig. 6 PXRD patterns of $\text{Na}_7[\text{SbW}_6\text{O}_{24}]$ before (black line) and after (red line) rehydration at a relative humidity (RH) level of 100% for three days at room temperature, compared with that of the $\text{Na}_7[\text{SbW}_6\text{O}_{24}] \cdot 16\text{H}_2\text{O}$ reference (blue line).

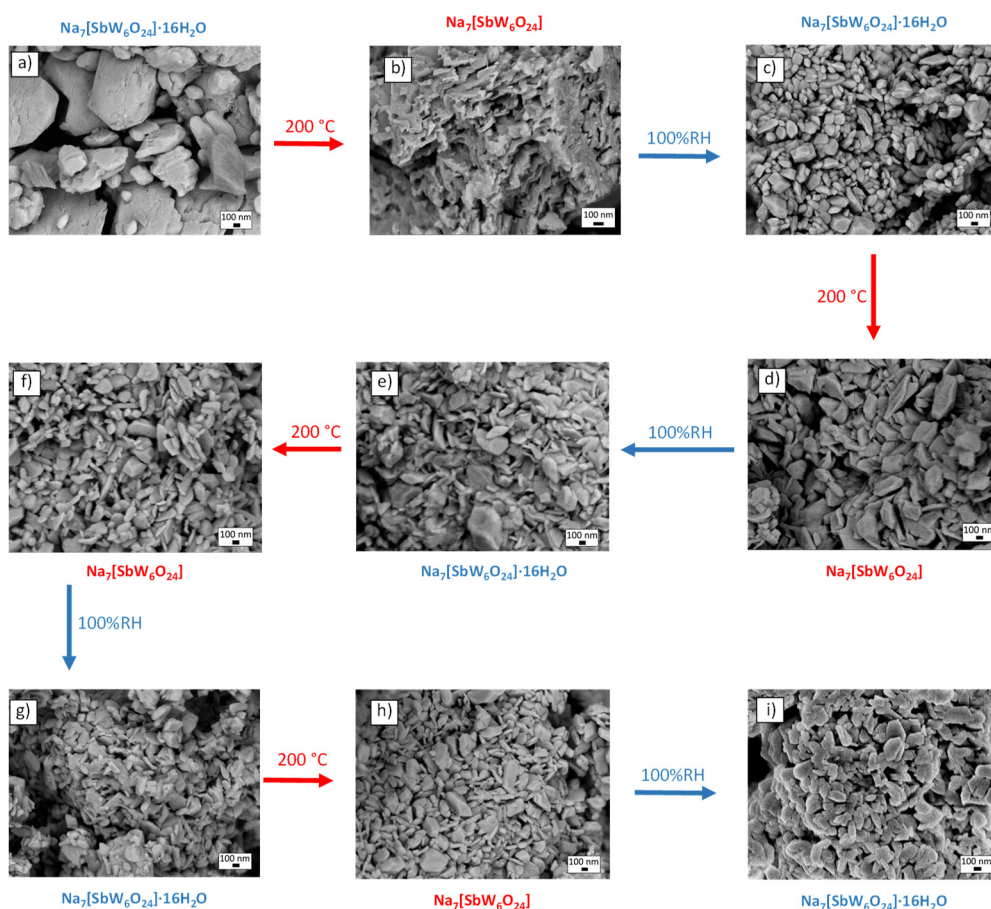


Fig. 7 SEM images of $\text{Na}_7[\text{SbW}_6\text{O}_{24}] \cdot 16\text{H}_2\text{O}$ and $\text{Na}_7[\text{SbW}_6\text{O}_{24}]$ particles during 4 successive cycles of thermal dehydration ($200\text{ }^\circ\text{C}$, 10 minutes)/rehydration (100% RH, 3 days) processes.

To complete this study, single-crystals of $\text{Na}_7[\text{SbW}_6\text{O}_{24}] \cdot 16\text{H}_2\text{O}$ were grind manually in a mortar, and the evolution of the particles size and morphology during successive dehydration/rehydration cycles was investigated in detail by SEM (Fig. 7). For each cycle, the hydrated phase was heated at 200 °C for 10 minutes and then, rehydrated upon exposure to moisture-laden air (100% RH) in a closed chamber for three days at room temperature. The evolution of the specific surface area of particles was also determined using the BET method. The starting particles of $\text{Na}_7[\text{SbW}_6\text{O}_{24}] \cdot 16\text{H}_2\text{O}$ have a fairly high size dispersion ranging from 150 nm to a few micrometers (Fig. 7a), associated to a low specific surface area of 2.53 m²/g. Then, the first thermal treatment induces a fragmentation of the particles leading to sizes of about 100-200 nm small particles of $\text{Na}_7[\text{SbW}_6\text{O}_{24}]$ (Fig. 7b). However, these particles are highly aggregated giving rise to only a weak increase in the specific surface area (3.00 m²/g). After complete rehydration, the particles are converted to very small faceted crystals of $\text{Na}_7[\text{SbW}_6\text{O}_{24}] \cdot 16\text{H}_2\text{O}$, quite homogeneous in shape and with a mean size in the 100-400 nm range (Fig. 7c). Interestingly, the associated specific surface area (10.00 m²/g) is higher than that of the starting particles of the hydrated compound. The second thermal treatment leads to small particles of $\text{Na}_7[\text{SbW}_6\text{O}_{24}]$ with a mean size comparable to that of their hydrated mother particles (Fig. 7d). Nevertheless, the particles of $\text{Na}_7[\text{SbW}_6\text{O}_{24}]$ are much less aggregated than those obtained directly after the first thermal treatment (Fig. 7b), resulting in a significant increase of the specific surface area which reaches 13.09 m²/g. Finally, no significant changes in the particles size and morphology of both hydrated and anhydrous phases are observed during other successive rehydration/dehydration processes (Fig. 7e-7i). Let us notice that, after one similar dehydration/rehydration cycle, $\text{K}_5\text{Na}_2[\text{SbW}_6\text{O}_{24}] \cdot 12\text{H}_2\text{O}$ exhibits a comparable behaviour, and a significant decrease in its particles size from few micrometers to about 100-200 nm (Fig. S16, ESI[†]). Finally, by adapting the rehydration protocol described above, the deuterated analogue of $\text{K}_5\text{Na}_2[\text{SbW}_6\text{O}_{24}] \cdot 12\text{H}_2\text{O}$ has been prepared in order to better evidence the impact of the crystallized water molecules on the PL properties of the hydrated compound (see section 3). Thus, a freshly thermally dehydrated $\text{K}_5\text{Na}_2[\text{SbW}_6\text{O}_{24}]$ powder sample was kept under N₂ atmosphere in a closed chamber containing heavy water, for five days at room temperature. The PXRD analysis (Fig. S17, ESI[†]) confirms that the obtained compound is well isostructural to $\text{K}_5\text{Na}_2[\text{SbW}_6\text{O}_{24}] \cdot 12\text{H}_2\text{O}$. In addition, the FTIR-ATR spectrum of the deuterated material clearly evidences the vibrational signatures of D₂O and, to a lesser extent, HDO molecules (Fig. S18, ESI[†]).

3. Solid-state photophysical properties

3.1. Absorption and emission properties

The solid-state photophysical properties of the hydrated and anhydrous alkali Ln-free POM materials have been thoroughly investigated and compared (Table 2). The absorption properties have been studied at room temperature by diffuse reflectance spectroscopy of microcrystalline powder. The absorption spectra of all materials (Fig. S19, ESI[†]) show a broad absorption band in the range 250-320 nm which is assigned to mixed intense O→W and O→Sb ligand-to-metal charge-transfer (LMCT) transitions. The optical band gap is of 296 nm (4.19 eV), 301 nm (4.12 eV) and 318 nm (3.90 eV) for $\text{Na}_7[\text{SbW}_6\text{O}_{24}] \cdot 16\text{H}_2\text{O}$, $\text{K}_5\text{Na}_2[\text{SbW}_6\text{O}_{24}] \cdot 12\text{H}_2\text{O}$ and $\text{K}_7[\text{SbW}_6\text{O}_{24}] \cdot 6\text{H}_2\text{O}$, respectively. Strikingly, the absorption threshold is systematically red shifted for their anhydrous analogues, and reach 346 nm (3.58 eV), 321 nm (3.86 eV) and 334 nm (3.71 eV) for $\text{Na}_7[\text{SbW}_6\text{O}_{24}]$, $\text{K}_5\text{Na}_2[\text{SbW}_6\text{O}_{24}]$ and $\text{K}_7[\text{SbW}_6\text{O}_{24}]$, respectively. This has been interpreted considering that the thermal treatment

increases the concentration of absorbing $[\text{SbW}_6\text{O}_{24}]^{7-}$ units in the crystal lattices, strengthening electrostatic anion-anion interactions. For example, the $[\text{SbW}_6\text{O}_{24}]^{7-}$ volume concentration shifts from 1.81 × 10⁻³ mol cm⁻³ in $\text{Na}_7[\text{SbW}_6\text{O}_{24}] \cdot 16\text{H}_2\text{O}$ to 3.20 × 10⁻³ mol cm⁻³ in $\text{Na}_7[\text{SbW}_6\text{O}_{24}]$ i.e., a significant increase of 77%. In addition, the removal of water molecules directly bonded to the alkali ions increases their polarizing power and strengthens electrostatic interactions with POMs. Both effects induce a broadening and a redshift of the lowest energy absorption band toward higher wavelength.⁴⁹

Upon irradiation at 254 nm with a standard UV lamp, $\text{Na}_7[\text{SbW}_6\text{O}_{24}] \cdot 16\text{H}_2\text{O}$, $\text{K}_5\text{Na}_2[\text{SbW}_6\text{O}_{24}] \cdot 12\text{H}_2\text{O}$ and $\text{K}_7[\text{SbW}_6\text{O}_{24}] \cdot 6\text{H}_2\text{O}$ exhibit a weakly intense greenish-white emission at room temperature, barely observable with naked eyes. Their steady-state photoluminescence excitation (PLE) and emission spectra are displayed in Fig. S20, ESI[†]. The PLE spectra monitored at 513 nm show a broad band peaking at 254 nm with a shoulder at about 290 nm. These bands are in well agreement with the LMCT transitions observed in the absorption spectra, and are mainly dominated by the ¹A_{1g} → ¹T_{1u} transition of the O→W charge transfer photoexcitation.³³ The PL spectra monitored at 254 nm show a broad and structureless band centered at 513 nm. This emission is associated to a very large stoke shift of about 20174 cm⁻¹, and is characterized by the Commission Internationale de l'Éclairage (CIE) chromaticity coordinates of (0.3019, 0.4002) for $\text{Na}_7[\text{SbW}_6\text{O}_{24}] \cdot 16\text{H}_2\text{O}$, (0.3123, 0.4092) for $\text{K}_5\text{Na}_2[\text{SbW}_6\text{O}_{24}] \cdot 12\text{H}_2\text{O}$ and (0.2958, 0.3950) for $\text{K}_7[\text{SbW}_6\text{O}_{24}] \cdot 6\text{H}_2\text{O}$ (Fig. S21, ESI[†]). It can be assigned to the ³T_{1u} → ¹A_{1g} transitions originating from the two O→W LMCT emitting triplet states of the $[\text{SbW}_6\text{O}_{24}]^{7-}$ unit.³⁴ In the case of $\text{Na}_7[\text{SbW}_6\text{O}_{24}] \cdot 16\text{H}_2\text{O}$, this transition exhibits a short photoluminescence lifetime of τ = 7.71 ± 0.09 μs (Fig. S22, ESI[†]) and a very low quantum yield (Φ_F < 1%). Comparable results have been obtained for $\text{K}_5\text{Na}_2[\text{SbW}_6\text{O}_{24}] \cdot 12\text{H}_2\text{O}$ (τ = 4.82 ± 0.49 μs, Φ_F < 1%) and $\text{K}_7[\text{SbW}_6\text{O}_{24}] \cdot 6\text{H}_2\text{O}$ (τ = 7.17 ± 0.14 μs, Φ_F < 1%) (Fig. S22, ESI[†]). As expected, the three hydrated materials exhibit very limited PL performances at room temperature. Considering the large amount of water molecules involved in H-bonding interactions with the POM surface in the crystal structures of $\text{Na}_7[\text{SbW}_6\text{O}_{24}] \cdot 16\text{H}_2\text{O}$ and $\text{K}_5\text{Na}_2[\text{SbW}_6\text{O}_{24}] \cdot 12\text{H}_2\text{O}$ (see section 1.2), the strong PL quenching can be attributed to consequent nonradiative de-excitation processes due to O-H vibrators connecting the {WO₆} octahedra. Indeed, the hydrogen bonding network between Ln-free POMs and the neighboring water molecules creates dipole-dipole interactions which expand the luminescent {WO₆} octahedral sphere and increases the rate of radiationless deactivation of the excited states.³⁴ To confirm this, the emission properties of $\text{K}_5\text{Na}_2[\text{SbW}_6\text{O}_{24}] \cdot 12\text{H}_2\text{O}$ have been compared to those of its deuterated isotope (see section 2.3), because D₂O is often reported as a much poorer quencher than H₂O.⁵⁰ Upon similar photoexcitation at λ_{ex} = 254 nm, the PL profiles of both compounds are roughly comparable (Fig. S23, ESI[†]), but the deuterated compound exhibits a little bit more intense emission characterized by a slightly longer luminescence lifetime of τ = 5.79 ± 0.26 μs. These results seem to confirm that nonradiative deactivation of the emitting triplet states in $\text{K}_5\text{Na}_2[\text{SbW}_6\text{O}_{24}] \cdot 12\text{H}_2\text{O}$ mainly occurs by multiphonon relaxation induced by O-H vibration modes.

Noticeably, upon similar photoexcitation (λ_{ex} = 254 nm) at room temperature, $\text{Na}_7[\text{SbW}_6\text{O}_{24}]$, $\text{K}_5\text{Na}_2[\text{SbW}_6\text{O}_{24}]$ and $\text{K}_7[\text{SbW}_6\text{O}_{24}]$ show tremendous luminescence enhancement which strongly contrasts with the weak PL responses of the hydrates series. In particular, $\text{Na}_7[\text{SbW}_6\text{O}_{24}]$ exhibits a highly bright greenish-white emission (Fig. 8a).

Table 2. Photophysical data of the considered anhydrous and hydrated alkali Ln-free POM materials.

	E_g [eV] ^a	λ_{em} [nm] ^b	τ [μ s] ^c	Φ_F [%] ^d	k_r [$\times 10^3$ s ⁻¹] ^e	k_{nr} [$\times 10^3$ s ⁻¹] ^f
Na₇[SbW₆O₂₄]\cdot16H₂O	4.19	513	7.71 \pm 0.09	< 1	-	129.7
Na₇[SbW₆O₂₄]	3.58	513	88.00 \pm 0.60	36	4.1	7.3
K₅Na₂[SbW₆O₂₄]\cdot12H₂O	4.12	513	4.82 \pm 0.49	< 1	-	207.5
K₅Na₂[SbW₆O₂₄]	3.86	513	54.01 \pm 0.35	9	1.7	16.8
K₇[SbW₆O₂₄]\cdot6H₂O	3.90	513	7.17 \pm 0.10	< 1	-	139.5
K₇[SbW₆O₂₄]	3.71	513	55.73 \pm 0.04	13	2.3	15.6

^aOptical band gap. ^bEmission maximum at $\lambda_{ex} = 254$ nm. ^cPhotoluminescence lifetime monitored at $\lambda_{ex} = 254$ nm. ^dPhotoluminescence quantum yield. ^eRadiative decay rate ($k_r = \Phi_F/\tau$). ^fNonradiative decay rate ($k_{nr} = 1/\tau - k_r$).

The PLE spectra of **Na₇[SbW₆O₂₄]** (Fig. 8b), and **K₅Na₂[SbW₆O₂₄]** and **K₇[SbW₆O₂₄]** (Fig. S24, ESI[†]) monitored at 513 nm are well comparable with those of their corresponding hydrates (Fig. S20, ESI[†]), indicating that the photoexcitation processes remain unchanged. Moreover, the PL spectrum of **Na₇[SbW₆O₂₄]** (Fig. 8b) and those of **K₅Na₂[SbW₆O₂₄]** and **K₇[SbW₆O₂₄]** (Fig. S24, ESI[†]) monitored at 254 nm show that both the position in energy and the shape of the PL band does not hardly vary after dehydration, resulting in a very slight variation of the CIE chromaticity coordinates of (0.2800, 0.3804) for **Na₇[SbW₆O₂₄]**, (0.2819, 0.3814) for **K₅Na₂[SbW₆O₂₄]** and (0.2690, 0.3705) for **K₇[SbW₆O₂₄]** (Fig. S25, ESI[†]). However, the photoluminescence lifetime of **Na₇[SbW₆O₂₄]** is increased tenfold ($\tau = 88.00 \pm 0.60$ μ s) in relation with that of **Na₇[SbW₆O₂₄] \cdot 16H₂O** ($\tau = 7.71 \pm 0.09$ μ s), and its luminescence quantum yield reaches 36 %. Although less pronounced, significant enhancement of the PL intensity is also observed for **K₅Na₂[SbW₆O₂₄]** ($\tau = 54.01 \pm 0.35$ μ s, $\Phi_F = 9$ %) and **K₇[SbW₆O₂₄]** ($\tau = 55.73 \pm 0.04$ μ s, $\Phi_F = 13$ %) in relation with their hydrated analogues (Fig. S24, ESI[†]).

Considering that the hydrated compounds exhibit very low quantum yields (<1%) at room temperature, their associated k_r values have been considered as negligible compared to k_{nr} ones.

$$\Phi_F = k_r / (k_r + k_{nr}) \quad (1)$$

$$k_{nr} = 1/\tau - k_r \quad (2)$$

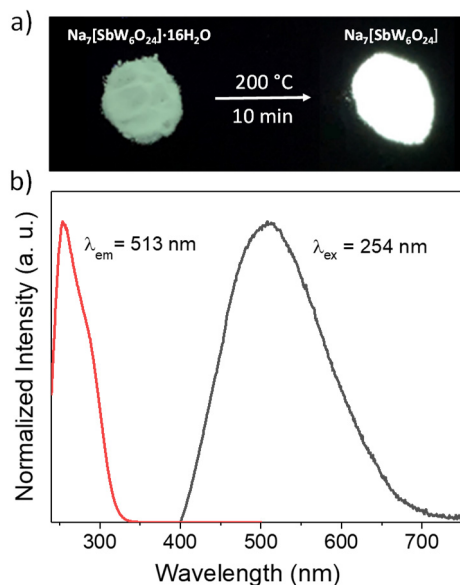


Fig. 8 (a) Photographs of **Na₇[SbW₆O₂₄] \cdot 16H₂O** and **Na₇[SbW₆O₂₄]** upon UV excitation ($\lambda_{ex} = 254$ nm) at room temperature. (b) Room-temperature excitation spectrum (red line) monitored at 513 nm and emission spectrum (black line) monitored at 254 nm of **Na₇[SbW₆O₂₄]**.

For both hydrated and anhydrous compounds, the excited state radiative (k_r) and nonradiative (k_{nr}) decay rates, extracted from equations (1) and (2), are gathered in Table 2 and depicted in Fig. 9.

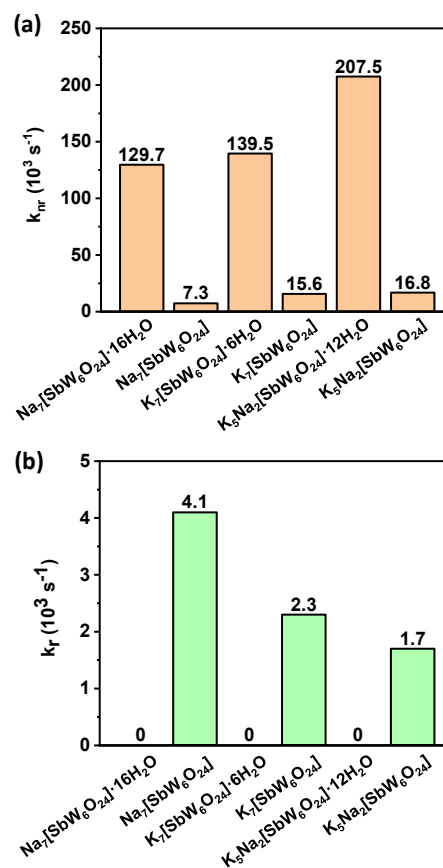


Fig. 9 Comparison of the excited state (a) radiative (k_r) and (b) nonradiative (k_{nr}) decay rates in the series of hydrated and anhydrous alkali Ln-free POM materials.

As expected, the nonradiative decay rates of the anhydrous compounds are extremely lower than those of the hydrated ones (Fig. 9a). For instance, k_{nr} is of 129.7×10^3 s⁻¹ for **Na₇[SbW₆O₂₄] \cdot 16H₂O** and is divided by a factor almost 18 for **Na₇[SbW₆O₂₄]** (7.3×10^3 s⁻¹).

Similarly, the k_{nr} values of $K_7[SbW_6O_{24}] \cdot 6H_2O$ ($139.5 \times 10^3 s^{-1}$) and of $K_5Na_2[SbW_6O_{24}] \cdot 12H_2O$ ($207.5 \times 10^3 s^{-1}$) significantly drop to $15.6 \times 10^3 s^{-1}$ and $16.8 \times 10^3 s^{-1}$ for $K_7[SbW_6O_{24}]$ and $K_5Na_2[SbW_6O_{24}]$, respectively. This well confirms that the thermal dehydration processes at 200 °C remove all nonradiative de-excitation pathways caused by O-H vibrators, strongly improving the PL performances of the alkali Ln-free POM materials at room temperature. Concurrently, the radiative decay rates of the anhydrous materials are much greater than those of their hydrated analogues (Fig. 9b) which is also in direct line with their brighter luminescence. Focusing now specifically on the series of anhydrous materials, k_r is almost two times higher for $Na_7[SbW_6O_{24}]$ ($4.1 \times 10^3 s^{-1}$) than for $K_5Na_2[SbW_6O_{24}]$ ($1.7 \times 10^3 s^{-1}$) and $K_7[SbW_6O_{24}]$ ($2.3 \times 10^3 s^{-1}$), whereas at the same time, k_{nr} is more than two-fold lower (Fig. 9a). This well evidences that radiative decay is more favored when $[SbW_6O_{24}]^{7-}$ is associated with only sodium ions in the crystal lattice. Thus, replacing K^+ ions by smaller Na^+ ones may increase the rigidity of the ionic structure of such materials, and could significantly reduce nonradiative de-excitation pathways, as already observed in other luminescent alkali tungstates and molybdates.^{51,52}

3.2. Reversible vapoluminescent properties

As described in section 2.3., $Na_7[SbW_6O_{24}]$, $K_5Na_2[SbW_6O_{24}]$ and $K_7[SbW_6O_{24}]$ are fully converted back into $Na_7[SbW_6O_{24}] \cdot 16H_2O$, $K_5Na_2[SbW_6O_{24}] \cdot 12H_2O$ and $K_7[SbW_6O_{24}] \cdot 6H_2O$, respectively when exposed to moisture-laden air (100% RH) for three days at room temperature. Noticeably, as shown in Fig. 10a for $Na_7[SbW_6O_{24}]$ and in Fig. S26, ESI† for $K_5Na_2[SbW_6O_{24}]$ and $K_7[SbW_6O_{24}]$, the rehydration processes are associated with strong and complete PL quenching effects at room temperature, due to the highly contrasted PL responses of both the anhydrous and hydrated compounds (see section 3.1.). These results evidence that the three anhydrous materials are highly reactive towards water molecules in the atmosphere that they are able to optically detect according to a PL turn-off mechanism. This differs from the vapoluminescence mechanism proposed for compounds $(TBA)_4[PW_{11}O_{39}Bi]$ and $(TBA)_5[PW_{11}O_{39}Pb]$ for which exposure to humidity induces significant modifications of the luminescence profiles resulting in emission color change.³³ Interestingly, on the considered time scales, $Na_7[SbW_6O_{24}]$, $K_5Na_2[SbW_6O_{24}]$ and $K_7[SbW_6O_{24}]$ have also a high chemical inertness towards other gaseous molecules present in the air (O_2 , CO_2 ...) likely to induce side PL quenching processes. Let us also notice that the complete regeneration of the PL-active anhydrous phases can be achieved by a simple thermal treatment at 200 °C for 10 minutes.

The kinetics of PL quenching upon rehydration of $Na_7[SbW_6O_{24}]$, $K_5Na_2[SbW_6O_{24}]$ and $K_7[SbW_6O_{24}]$ have been investigated at room temperature. Single crystals of $Na_7[SbW_6O_{24}] \cdot 16H_2O$ and $K_7[SbW_6O_{24}] \cdot 6H_2O$, and the microcrystalline powder of $K_5Na_2[SbW_6O_{24}] \cdot 12H_2O$ were grind manually in a mortar, and then heated at 200 °C for 10 minutes. The obtained anhydrous materials were kept at room temperature in a closed chamber at 100% RH. Samples (60 mg) were collected at different exposure time, and their PL spectra were monitored (Fig. S27, ESI†). The temporal evolution of the percentages of PL intensity loss are displayed in Fig. 10b. The rehydration rates of the samples were compared by considering their PL quenching half-life time ($t_{1/2}$), namely the time required for the PL intensity loss to reach half of its final value. The $t_{1/2}$ values are short for $K_5Na_2[SbW_6O_{24}]$ (42 s) and $K_7[SbW_6O_{24}]$ (7.8 min), and the PL intensity loss is complete for about 60 min. In contrast, the $t_{1/2}$ value is much longer for $Na_7[SbW_6O_{24}]$ (49.5 min), and the PL intensity loss reaches 99 % for 8 hours. As an example, the PXRD pattern of

$K_5Na_2[SbW_6O_{24}]$ exposed upon 100% RH for 60 min well confirms the complete regeneration of $K_5Na_2[SbW_6O_{24}] \cdot 12H_2O$ (Fig. S28, ESI†).

This kinetics study shows that although the three anhydrous materials are isostructural, their rehydration rates strongly vary with the nature of the alkali ions. The fast PL quenching effects of $K_5Na_2[SbW_6O_{24}]$ and $K_7[SbW_6O_{24}]$ indicates that the regeneration of $K_5Na_2[SbW_6O_{24}] \cdot 12H_2O$ and $K_7[SbW_6O_{24}] \cdot 6H_2O$ occurs very quickly, while upon similar conditions, the conversion from $Na_7[SbW_6O_{24}]$ to $Na_7[SbW_6O_{24}] \cdot 16H_2O$ is much slower. If further investigations are still needed to fully rationalize the dehydration/rehydration mechanisms of these alkali POM salts, structural filiations between hydrated and anhydrous phases could be one of the key parameters that control their rehydration kinetics. Indeed, as discussed in section 2.1., the structures of $K_5Na_2[SbW_6O_{24}] \cdot 12H_2O$ and $K_5Na_2[SbW_6O_{24}]$ show strong similarities in the arrangement of POMs and alkali ions into alternated hexagonal supramolecular layers stacked along the *c*-axis. Thus, the incorporation of water molecules into the crystal lattice of $K_5Na_2[SbW_6O_{24}]$ could involve very limited structural reorganization resulting in fast rehydration processes. In strong contrast, the phase transformation from $Na_7[SbW_6O_{24}]$ to $Na_7[SbW_6O_{24}] \cdot 16H_2O$ implies breaking the layered structures and significant rearrangements of both anionic and cationic species which could be in direct line with the slower rehydration of the anhydrous sodium compound.

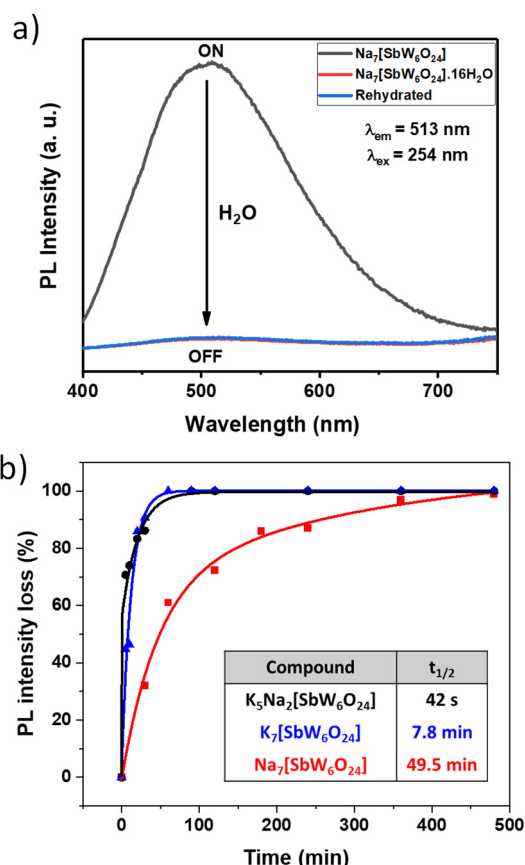


Fig. 10 (a) Room-temperature PL spectra monitored at 254 nm of $Na_7[SbW_6O_{24}]$ before (black line) and after (blue line) rehydration for three days at 100% RH, compared with that of pristine $Na_7[SbW_6O_{24}] \cdot 16H_2O$ (red line). (b) Evolution of the percentage of PL intensity loss of $Na_7[SbW_6O_{24}]$ (red square), $K_5Na_2[SbW_6O_{24}]$ (black square) and $K_7[SbW_6O_{24}]$ (blue square). Solid lines are guides for the eyes. Inset: PL quenching half-life times of the different anhydrous materials.

EXPERIMENTAL SECTION

Synthesis. All reagents and solvents used were commercially available.

Na₇[SbW₆O₂₄]·16H₂O. Na₂WO₄·2H₂O (2 g, 6 mmol) was dissolved in 40 ml of water. After addition of SbCl₅ (190 μL, 1.5 mmol), the pH of the colorless solution was adjusted to 7 by adding hydrochloric acid (4M) dropwise. The solution was heated to 85 °C until three quarters of the volume remained. The solution was cooled down to room temperature and then filtrated. The filtrate was left at room temperature, and colourless plate-like crystals were obtained after one week. Yield in W: 46%. FT-IR (KBr pellet, cm⁻¹) H₂O 3465 (m), 1630 (m); [SbW₆O₂₄]⁷⁻ 955 (m), 935 (s), 891 (s), 872 (s), 675 (s), 602 (m), 451 (s).

K₅Na₂[SbW₆O₂₄]·12H₂O. K₂WO₄ (988 mg, 3 mmol) was dissolved in 20 mL of water. After addition of K₂Sb(OH)₆ (132 mg, 0.5 mmol) and NaCl (116.8 mg, 2 mmol), the pH of the colorless solution was adjusted to 7 by adding hydrochloric acid (4M) dropwise. The solution was heated at 85 °C until three quarters of the volume remained. A white precipitate is obtained during the heating. The solution was cooled down to room temperature and then filtrated. A white microcrystalline powder is obtained and washed with cold water. Yield in W: 77%. FT-IR (KBr pellet, cm⁻¹) H₂O 3516 (m), 1630 (m); [SbW₆O₂₄]⁷⁻ 932 (s), 887 (s), 702 (m), 604 (s), 571 (s), 451 (s).

K₇[SbW₆O₂₄]·6H₂O. K₂WO₄ (988 mg, 3 mmol) was dissolved in 20 mL of water. After addition of K₂Sb(OH)₆ (132 mg, 0.5 mmol), the pH of the colorless solution was adjusted to 7 by adding hydrochloric acid (4M) dropwise. The solution was heated to 85 °C until three quarters of the volume remained. The solution was cooled down to room temperature and then filtrated. The filtrate was left at room temperature and highly efflorescent colourless plate-like crystals were obtained after two days. Yield in W: 63%. FT-IR (KBr pellet cm⁻¹) H₂O 3454 (m), 1651 (m); [SbW₆O₂₄]⁷⁻ 935 (s), 885 (s), 683 (s), 571 (s), 449 (m).

Na₇[SbW₆O₂₄], K₅Na₂[SbW₆O₂₄] and K₇[SbW₆O₂₄]. Single-crystals of Na₇[SbW₆O₂₄]·16H₂O and K₇[SbW₆O₂₄]·6H₂O or microcrystalline powder of K₅Na₂[SbW₆O₂₄]·12H₂O were grind manually in a mortar, and the obtained white powders were heated at 200 °C in an oven for 10 minutes. FTIR-ATR Na₇[SbW₆O₂₄]: 953 (s), 872 (s), 652 (s), 615 (m), 578 (m), 493 (s), 450 (s). K₅Na₂[SbW₆O₂₄]: 940 (s), 866 (s), 648 (m), 600 (s), 567 (s), 487 (s), 446 (s). K₇[SbW₆O₂₄]: 940 (s), 866 (m), 652 (m), 600 (m), 569 (s), 487 (s), 450 (s).

Physical measurements. Fourier transform infrared (FT-IR) and Fourier transform infrared with attenuated total reflectance (FTIR-ATR) spectra were recorded in the 4000-400 cm⁻¹ range on a BRUKER Vertex equipped with a computer control using the OPUS software. Fourier transform Raman (FT-Raman) spectra were collected at room temperature under an excitation wavelength of 1064 nm (Nd:YAG laser) using a FT-Raman Bruker RFS 100 spectrophotometer. The nominal power was 300 mW. Solid-state FT-Raman spectra were recorded at 4 cm⁻¹ resolution over the wavenumber range 3-4000 cm⁻¹, with 100 scan accumulation. Differential scanning calorimetry (DSC) and thermogravimetric analysis (TGA) were performed by flowing air with a heating and cooling rate of 5°C/min on a SETARAM TG-DSC 111 between room temperature and 800 °C. Powder X-ray Diffraction (PXRD) patterns were collected at room temperature on a Bruker D8 Advance instrument in the Bragg-Brentano geometry, equipped with a front germanium monochromator, a copper anode

(CuK-L3 radiation λ=1.540598 Å) and a LynxEye PSD detector. Scanning Transmission Electron Microscopy (S/TEM) characterization was performed on a Cs-probe corrected Themis Z G3 (Thermo Fisher Scientific) operating at 80 kV accelerating voltage. High Angle Annular Dark Field (HAADF) images were acquired with a 30.5 mrad convergence angle and 50 - 200 mrad collection angles and Energy Dispersive X-ray Spectroscopy (EDS) maps were acquired with 4 windowless silicon drift detectors (Super-X system). HT-PXRD experiments were carried out on a Bruker D8 Advance instrument using Cu K-L2-L3 (λ = 1.540598, 1.54433 Å) radiation and a Vântec PSD detector. The morphology of powder was investigated with a field-emission gun scanning electron microscope JEOL JSM7600F operating at 7 kV. Density measurements were collected at room temperature on an AccuPyc II 1340 V1.09 with helium as analysis gas. Nitrogen volumetric measurements treated by the Brunauer-Emmett-Teller (BET) approaches were collected on a TriStar II 3020 device. Diffuse reflectance spectra were collected at room temperature on a finely ground sample with a Perkin-Elmer Lambda 1050 spectrometer equipped with a 150 mm diameter integrating sphere coated with Spectralon®, a highly reflecting fluoropolymer. Diffuse reflectance was measured from 250 to 1000 nm with a 2 nm step using Spectralon® as reference (100% reflectance). The reflectance data were treated by a Kubelka-Munk transformation⁴¹ to better determine the absorption thresholds. Room-temperature photoluminescence spectra were recorded on a Jobin-Yvon Fluorolog 3 fluorometer equipped with a photomultiplier (excitation source: 400 W Xe arc lamp and 150W pulsed map for decay times). The emission spectra were corrected for detection and optical spectral response of the spectrofluorimeter and the excitation spectra were weighed for the spectral distribution of the lamp intensity using a photodiode reference detector. Quantum yields were recorded on a Jasco FP-8500 spectrofluorometer equipped with an integrating sphere ILF-835 (100 mm).

Conclusions

In summary, three new water-responsive luminescent alkali Ln-free POM materials Na₇[SbW₆O₂₄], K₅Na₂[SbW₆O₂₄] and K₇[SbW₆O₂₄] have been successfully elaborated by thermally dehydrating at 200 °C Na₇[SbW₆O₂₄]·16H₂O, K₅Na₂[SbW₆O₂₄]·12H₂O and K₇[SbW₆O₂₄]·6H₂O. The structures of the isostructural anhydrous compounds have been solved from *ab initio* powder X-ray diffraction determination. FTIR-ATR and FT-Raman spectroscopy analyses have also confirmed the integrity of the [SbW₆O₂₄]⁷⁻ unit after the thermal treatment. The three hydrates are weakly or nonluminescent at room temperature (Φ_F < 1 %), because crystallized water molecules connecting the oxygen POM surface through complex H-bonding networks promote non-radiative deactivation processes from the O→W charge-transfer emitting triplet states by multiphonon relaxation. However, after complete thermal dehydration, the anhydrous phases exhibit a tremendous solid-state photoluminescence enhancement, in direct line with a significant decrease in the excited state nonradiative decay rates due to the removal of all O-H vibrators. In this series, the PL quantum yield is greater for Na₇[SbW₆O₂₄] (Φ_F = 36 %) than for K₇[SbW₆O₂₄] (Φ_F = 13 %) and K₅Na₂[SbW₆O₂₄] (Φ_F = 9 %), underlining that the substitution of K⁺ by Na⁺ ions strengthens the rigidity of the ionic structure and directs favorably the

balance between radiative and nonradiative de-excitation processes. Noticeably, the three anhydrous materials exhibit efficient vapoluminescence properties upon exposure to a humid atmosphere (100% RH). They are fully converted back into their hydrated analogues, and the phase transformations are accompanied by strong and complete PL quenching effects. This stands as the first family of Ln-free POM-based materials able to detect water according to a PL turn-off mechanism. The rehydration rates are faster for $\text{K}_5\text{Na}_2[\text{SbW}_6\text{O}_{24}]$ and $\text{K}_7[\text{SbW}_6\text{O}_{24}]$ than for $\text{Na}_7[\text{SbW}_6\text{O}_{24}]$, and seems strongly correlate to the existence of structural filiations between the anhydrous materials and their hydrates. Finally, after use, the PL-active anhydrous phases can be easily regenerated by a fast thermal treatment at 200 °C. Further investigations are currently under study in our group to fully rationalize the hydration/dehydration mechanisms of these materials. In addition, these results open the way towards new fields of optical applications for alkali Ln-free POM materials. In particular, the drastic and reversible modulation in PL quantum efficiency of $\text{Na}_7[\text{SbW}_6\text{O}_{24}]$, $\text{K}_7[\text{SbW}_6\text{O}_{24}]$ and $\text{K}_5\text{Na}_2[\text{SbW}_6\text{O}_{24}]$ can be appropriately profiled to design new robust and reusable water-responsive luminescent materials for anticounterfeiting technologies and turn off-on PL sensing of RH in the atmosphere.

Author Contributions

The manuscript was written through contributions of all authors. All authors have given approval to the final version of the manuscript.

Conflicts of interest

There are no conflicts to declare.

Acknowledgements

This work was supported by the CNRS, Nantes Université, the Région des Pays de la Loire and the Ministère de l'Enseignement Supérieur et de la Recherche. The CIMEN Electron Microscopy Center in Nantes is also greatly acknowledged. The authors would like to thank Pr. Pierre Frère and Nagham Ibrahim (Moltech-Anjou, University of Angers, France) for their expert assistances in the characterization of luminescence quantum yield measurements.

References

- 1 E. Coronado, C. J. Gómez-García, *Chem. Rev.* 1998, **98**, 273–296.
- 2 J. M. Cameron, G. Guillemot, T. Galambos, S. S. Amin, E. Hampson, K. M. Haidaraly, G. N. Newton, G. Izzet, *Chem. Soc. Rev.* 2022, **51**, 293–328.
- 3 J. J. Baldoví, Y. Duan, C. Bustos, S. Cardona-Serra, P. Gouzerh, R. Villanneau, G. Gontard, J. M. Clemente-Juan, A. Gaita-Ariño, C. Giménez-Saiz, A. Proust, A. Coronado, *Dalton Trans.* 2016, **45**, 16653–16660.
- 4 J. M. Clemente-Juan, E. Coronado, A. Gaita-Ariño, *Chem. Soc. Rev.* 2012, **41**, 7464–7478.
- 5 M. S. Wang, G. Xu, Z. J. Zhang, G. C. Guo, *Chem. Commun.* 2010, **46**, 361–376.
- 6 O. Stetsiuk, P. Bolle, M. Cordier, J. Boixel, R. Dessapt, *J. Mater. Chem. C* 2022, **10**, 899–907.
- 7 P. Mialane, C. Mellot-Draznieks, P. Gairola, M. Duguet, Y. Benseghir, O. Oms, A. Dolbecq, *Chem. Soc. Rev.* 2021, **50**, 6152–6220.
- 8 J. Gu, W. Chen, G. G. Shan, G. Li, C. Sun, X. L. Wang, Z. Su, *Mater. Today Energy* 2021, **21**, 100760.
- 9 K. Suzuki, N. Mizuno, K. Yamaguchi, *ACS Catal.* 2018, **8**, 10809–10825.
- 10 C. Boglio, G. Lemièrre, B. Hasenknopf, S. Thorimbert, E. Lacôte, M. Malacria, *Angew. Chem. Int. Ed.* 2006, **45**, 3324–3327.
- 11 T. Yamase, T. Kobayashi, M. Sugeta, H. Naruke, *J. Phys. Chem. A* 1997, **101**, 5046–5053.
- 12 Q. Li, D. Wang, X. Fang, X. Wang, S. Mao, K. Ostrikov, *Adv. Funct. Mater.* 2021, **31**, 2104572.
- 13 C. Boskovic, *Acc. Chem. Res.* 2017, **50**, 2205–2214.
- 14 A. M. Kaczmarek, J. Liu, B. Laforce, L. Vincze, K. V. Hecke, R. V. Deun, *Dalton Trans.* 2017, **46**, 5781–5785.
- 15 Y. Zhao, S. Chen, Y. Ji, V. Singh, P. Ma, J. Lu, J. Niu, J. Wang, *CrystEngComm* 2019, **21**, 3627–3633.
- 16 D. Drewes, E. Melanie Limanski, B. Krebs, *Dalton Trans.* 2004, **0**, 2087–2091.
- 17 L. Ni, F. Hussain, B. Spingler, S. Weyeneth, G. R. Patzke, *Inorg. Chem.* 2011, **50**, 4944–4955.
- 18 W. Salomon, A. Dolbecq, C. Roch-Marchal, G. Paille, R. Dessapt, P. Mialane, H. Serier-Brault, *Front. Chem.* 2018, **6**, 188–195.
- 19 L. Jiang, J. Li, D. Xia, M. Gao, W. Li, D. Y. Fu, S. Zhao, G. Li, *ACS Appl. Mater. Interfaces* 2021, **13**, 49462–49471.
- 20 T. Zhang, H. W. Li, Y. Wu, Y. Wang, L. Wu, *J. Phys. Chem. C* 2015, **119**, 8321–8328.
- 21 A. S. Holmes-Smith, J. Crisp, F. Hussain, G. R. Patzke, G. Hungerford, *ChemPhysChem* 2016, **17**, 418–424.
- 22 G. Blasse, G. J. Dirksen, F. Zonnevijlle, *J. Inorg. Nucl. Chem.* 1981, **43**, 2847–2853.
- 23 H. Wu, M. Zhi, V. Singh, H. Li, P. Ma, J. Niu, J. Wang, *Dalton Trans.* 2018, **47**, 13949–13956.
- 24 D. F. Shen, S. Li, H. Liu, W. Jiang, Q. Zhang, G. G. Gao, *J. Mater. Chem. C* 2015, **3**, 12090–12097.
- 25 P. Sun, S. Zhang, Z. Xiang, T. Zhao, D. Sun, G. Zhang, M. Chen, K. Guo, X. Xin, *J. Colloid Interface Sci.* 2019, **547**, 60–68.
- 26 J. Lu, Q. Kang, J. Xiao, T. Wang, M. Fang, L. Yu, *Carbohydr. Polym.* 2018, **200**, 560–566.
- 27 Y. Guo, J. Lu, Q. Kang, M. Fang, L. Yu, *Langmuir* 2018, **34**, 9195–9202.
- 28 Y. Liu, X. Yuan, W. Wang, Y. Wu, L. Wu, *New J. Chem.* 2018, **42**, 17339–17345.
- 29 N. Lei, D. Shen, X. Chen, *Soft Matter* 2019, **15**, 399–407.
- 30 Y. F. Qiu, H. Liu, J. X. Liu, C. Zhang, Z. Ma, P. A. Hu, G. G. Gao, *J. Mater. Chem. C* 2015, **3**, 6322–6328.
- 31 P. Bolle, N. Albrecht, T. Amiaud, B. Humbert, E. Faulques, R. Dessapt, H. Serier-Brault, *Inorg. Chem.* 2019, **58**, 16322–16325.
- 32 C. M. Granadeiro, R. A. Sá Ferreira, P. C. R. Soares-Santos, L. D. Carlos, H. I. S. Nogueira, *J. Alloys Compd.* 2008, **451**, 422–425.
- 33 A. A. Mukhacheva, T. Asanova, M. R. Ryzhikov, T. S. Sukhikh, N. B. Kompankov, V. V. Yanshole, A. S. Berezin, A. L. Gushchin, P. A. Abramov, M. N. Sokolov, *Dalton trans.* 2021, **50**, 6913–6922.
- 34 T. Yamase, M. Sugeta, *J. Chem. Soc., Dalton trans.* 1993, **0**, 759–765.
- 35 T. Yamase, *Mol. Eng.* 1993, **3**, 241–262.

- 36 T. Yamase, T. Kobayashi, S. F. A. Kettle, *J. Electrochem. Soc.* 1996, **143**, 1678-1680.
- 37 T. Ito, H. Yashiro, T. Yamase, *Langmuir* 2006, **22**, 2806–2810.
- 38 H. Naruke, T. Yamase, *Acta crystallogr., C Cryst. struct. commun.* 1992, **48**, 597–599.
- 39 A. A. Mukhacheva, P. A. Abramov, M. N. Sokolov, *Curr. Inorg. Chem.* 2018, **7**, 4-7.
- 40 U. Lee, Y. Sasaki, *Bull. Korean Chem. Soc.* 1987, **8**, 1–3.
- 41 P. Kubelka, *Z. Tech. Phys.* 1931, **12**, 593–601.
- 42 H. M. Rietveld, *J. Appl. Crystallogr.* 1969, **2**, 65–71.
- 43 A. Altomare, C. Cuocci, C. Giacovazzo, A. Moliterni, R. Rizzi, N. Corriero, A. Falcicchio, *J. Appl. Crystallogr.* 2013, **46**, 1231–1235.
- 44 A. Boultif, D. Louër, *J. Appl. Crystallogr.* 2004, **37**, 724–731.
- 45 R. Černý, V. Favre-Nicolin, *Z. Kristallogr. Cryst. Mater.* 2007, **222**, 105–113.
- 46 B. L. George, G. Aruldas, I. L. Botto, *J. Mater. Sci. Lett.* 1992, **11**, 1421-1423.
- 47 C. Rocchiccioli-Deltcheff, M. Fournier, *J. Chem. Soc. Faraday Trans.* 1991, **87**, 3913–3920.
- 48 M. H. Alizadeh, A. R. Salimi, *Spectrochim. Acta A Mol. Biomol. Spectrosc.* 2006, **65**, 1104–1111.
- 49 M. Fournier, C. Louis, M. Che, P. Chaquin, D. Masure, *J. Catal.* 1989, **119**, 400–414.
- 50 J. L. Kropp, M. W. Windsor, *J. Chem. Phys.* 1965, **42**, 1599–1608.
- 51 C. Guo, S. Wang, T. Chen, L. Luan, Y. Xu, *Appl. Phys. A* 2009, **94**, 365–371.
- 52 J. Kim, *Inorg. Chem.* 2017, **56**, 8078–8086.